Nuclear Instruments and Methods in Physics Research B 267 (2009) 2680–2689

Contents lists available at ScienceDirect

Nuclear Instruments and Methods in Physics Research B

journal homepage: www.elsevier.com/locate/nimb

Mechanisms of damage formation in semiconductors

E. Wendler

Friedrich-Schiller-Universität Jena, Institut für Festkörperphysik, Max-Wien-Platz 1, 07743 Jena, Germany

ARTICLE INFO

Article history:
Available online 2 June 2009

PACS:
61.80.Jh
61.82.Fk
61.80.Az

Keywords:
Ion implantation
Radiation damage
Amorphization
Semiconductors

ABSTRACT

The damage accumulation in ion-implanted semiconductors is analysed using Rutherford backscattering spectrometry (RBS). When energetic ions are implanted in a material, they transfer their energy mainly into atomic collision processes (nuclear energy loss) and in electronic excitations (electronic energy loss). For a given material this primary energy deposition is determined by the mass and energy of the implanted ions and the ion fluence (number of ions per unit area). However, the damage concentration which is measured after implantation does not only depend on the primary energy deposition, but is strongly influenced by secondary effects like defect annealing and defect transformation. For the latter processes the target temperature and the ion flux (number of ions per unit area and time) play an important role. In this presentation the influence of the various parameters mentioned above on the damage accumulation is demonstrated for various materials. Simple empirical models are applied to get information about the processes occurring and to systematize the results for the various semiconductors.

1. Introduction

Much work has been done on radiation damage due to ion implantation, especially in semiconductors in the last nearly 50 years, and it is neither possible nor is it the aim here to summarise all that research. The paper is rather an attempt to show trends, how the various irradiation parameters influence the formation of radiation damage and to what extent the results for various semiconductors can be generalised, mainly referring to the work of the Jena group. Of course, it is beyond controversy that different microscopic mechanisms occur during ion implantation in the various materials.

Radiation damage is, strictly speaking, a disturbance of the periodic order of the lattice atoms in the crystalline materials. It therefore changes many properties that can be taken as a measure for the radiation damage produced. Most commonly these are electrical properties (e.g. charge carrier concentration and mobility, energy levels within the forbidden energy gap), optical properties (e.g. absorption coefficient, refractive index) or mechanical properties (e.g. hardness, curvature). Especially important for the defect analysis is transmission electron microscopy (TEM), because it gives direct images of the radiation damage. Another technique widely used to study ion-implanted semiconductors is Rutherford backscattering spectrometry (RBS). Most of the data presented here result from RBS. For a detailed description of this method the reader is referred to [1,2]. For the understanding of the following text it is important to know that with RBS the relative concentration of uncorrelated displaced lattice atoms (being randomly distributed within the lattice cell), n_{da}, can be determined as a function of the depth z [3]. For short $n_{da}(z)$ is called the defect or damage concentration. The value $n_{da} = 1$ is commonly taken as indication of amorphization.

2. Relevant parameters

The parameters relevant to the formation of radiation damage are the ion mass, the target temperature during irradiation, T_I, the ion flux j (number of implanted ions per unit area and time), the ion energy and the ion fluence N_I (number of ions per unit area). In this section the influence of these parameters on the damage formation is demonstrated by means of selected examples.

2.1. Ion mass

The ion mass strongly determines the energy transferred to the crystal lattice. The ions lose their energy by excitation of the electronic system (electronic energy loss) and through nuclear collisions with the host atoms (nuclear energy loss), and finally come to rest at a certain depth z (see e.g. [1]). It is common practice to recalculate the energy deposited per ion and unit length in collision processes into the number of primary displacements per ion and unit length, N^*_{displ}, because for many materials reasonable data for the displacement energies do exist (see Table 1). These primary effects can be calculated with the computer code SRIM [4]. An example for such calculations is given in Fig. 1, which compares

E-mail address: elke.wendler@uni-jena.de

0168-583X/$ - see front matter © 2009 Elsevier B.V. All rights reserved.
doi:10.1016/j.nimb.2009.05.059

Table 1
Displacement energies E_d obtained from MD simulations (calc.) or from experiments (exp.) (first/ second component). See also the references within the cited references.

Material	E_d(eV) (calc.)	E_d(eV) (exp.)	Reference
AlAs	25/20	–	[10]
GaN	45/109	41/–	[8,9]
GaP	–	13.7/19.2	[11]
GaAs	14/14	8.8/10.1	[10,12]
GaSb	–	6.2/(7.5–13.1)	[13]
InP	–	6.6/8.8	[12]
InAs	–	6.7/8.5	[12]
InSb	–	5.8/6.8	[12]
SiC	35/21	(20–35)/–	[14–16]
Si	15–20	13–14	[17–19]
Ge	–	14.5–16	[18,20]
ZnO	–	(40–70)/(47–55)	[21,22]
MgO	–	55/55	[21]

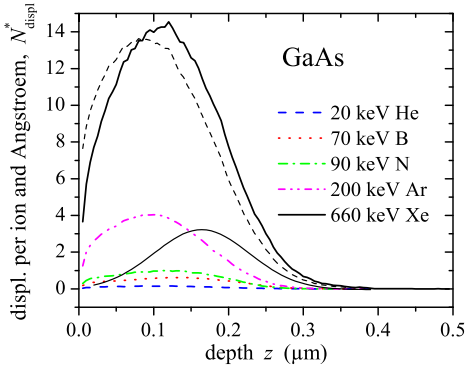

Fig. 1. Number of primary displacements per ion and unit length, N^*_{displ}, versus depth z for various ion species implanted in GaAs. For Xe ions, the electronic energy loss (thin dashed line) and the ion distribution (thin solid line) are included in arbitrary units.

the depth distribution of N^*_{displ} for various ion species implanted into GaAs. The ion energies were chosen to realize the maximum at a similar depth. Additionally the electronic energy loss and the ion distribution are given for the case of Xe. Fig. 1 shows that the value of N^*_{displ} in the maximum of the distribution increases with rising ion mass. Because N^*_{displ} reflects the effect of a single ion impact, more damage is to be expected for heavier ions. For irradiation energies up to a few 100 keV, under consideration here, the depth distributions of nuclear and electronic energy loss are rather close to each other. Therefore, their influence on the damage formation can not be distinguished. Of course, the main damage is produced by the nuclear energy loss which results in collision cascades, the density of which depends on the ion mass (see Fig. 1). The electronic energy loss itself is too low to produce damage in semiconductors [5]. Nevertheless, the electronic energy may influence the effect of the nuclear energy loss (see Section 4).

When a certain ion fluence N_I is applied, the total number of displacements per volume is given by the product $N^*_{displ}N_I$. Normalisation of this quantity to the atomic density N_0 of the corresponding material yields the number of displacements per lattice atom, n_{dpa}, with $n_{dpa} = N^*_{displ}N_I/N_0$. For example, a value of $n_{dpa} = 0.1$ means that so much energy was deposited in collision processes that in principle 10% of all lattice atoms could be displaced. n_{dpa} is also referred to as normalised ion fluence. It allows for comparison of the results for different ion species implanted into one material, or for one ion species into various materials.

To demonstrate the effect of the ion mass, various ion species were implanted with the ion fluences adjusted to realize equal values of n_{dpa} in the maximum of the distribution. The result of such experiments is shown in Fig. 2 for GaN [6] and GaAs [7]. In both cases implantation and defect analysis were done at a very low temperature to widely exclude thermal effects. In the case of GaN, within the experimental uncertainty, for all ion species applied, the same amount of damage is produced (see Fig. 2(a)). This means that in GaN – at the corresponding state of damaging – no effect of the ion species itself occurs, but only the energy density deposited into nuclear processes is of importance. The behaviour is completely different in the case of GaAs (see Fig. 2(b)). Here, despite the equal n_{dpa} values, the ion mass itself clearly influences the damage production. Much more damage is observed for the heavier ions. A more detailed discussion of these effects is given in Sections 4 and 7.2.

2.2. Implantation temperature

With increasing temperature intrinsic defects (vacancies or interstitials) may become mobile. This allows for defect recombination within the primary collision cascades, which reduces the damage remaining after implantation. A typical example to illustrate this is shown in Fig. 3, which plots the damage concentration for Si implanted InP as a function of the implantation temperature [23]. At temperatures up to room temperature an amorphous layer is formed and for $T_I > 300$ K the damage concentration decreases rapidly. The result indicates already the existence of a critical range of T_I, which will be discussed in detail in Section 3. Implantation at elevated temperatures [24] is also connected with a change of the type of defects. At these temperatures for low ion fluences, mainly point defects and point defect complexes are to be expected, which may transform to complex structures at high ion fluences, consisting of a mixture of defect clusters and extended defects. In this case the ions themselves start to play a prominent role in the process of damage formation. Further one can observe strong deviations between the shape of the damage profiles calculated with SRIM and that of the measured ones, suggesting the annealing to be

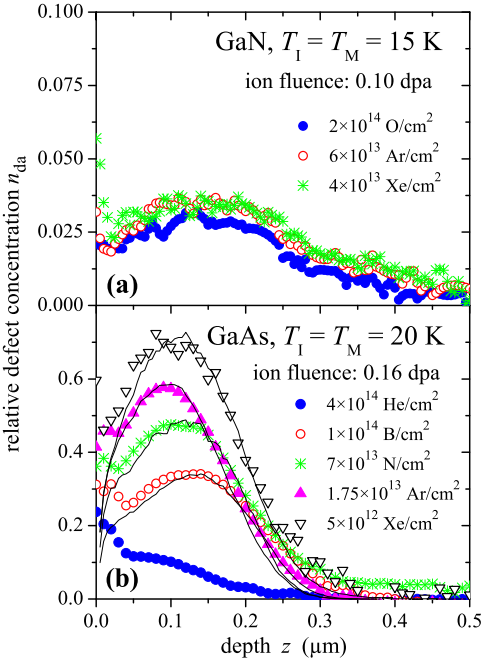

Fig. 2. Damage profiles $n_{da}(z)$ for GaN (a) and GaAs (b) implanted and measured at a very low temperature and using various ion species. The thin lines in part (b) are the lattice displacements (see Fig. 1) normalised to fit the corresponding maximum values.

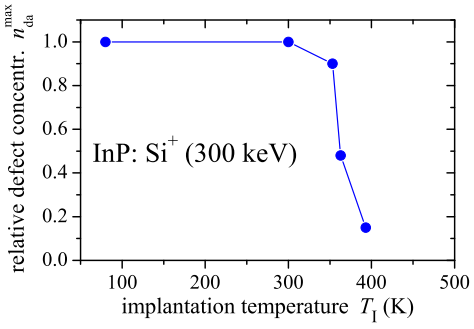

Fig. 3. Relative defect concentration in the maximum of the distribution, n_{da}^{max}, as a function of the implantation temperature T_I for InP implanted with Si ions using an ion fluence of $N_I = 2 \times 10^{14}$ cm^{-2}.

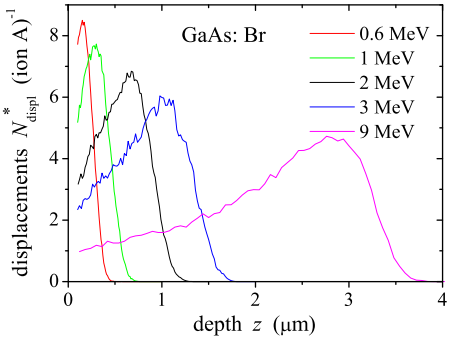

Fig. 5. Number of primary displacements per ion and unit length, N^*_{displ}, versus depth z for Br ions implanted in GaAs with various ion energies.

especially pronounced at the interface between implanted layer and underlying crystalline substrate (see Section 5).

2.3. Ion flux

The ion flux is the number of ions implanted per unit area and time. Thus it determines the time between two subsequent ion impacts. This time is available for annealing of the damage produced by the previous ion. A high ion flux may also locally warm the sample. Therefore, the effect of the ion flux on the formation of radiation damage is closely related to the implantation temperature T_I and it is often hard to differentiate between them. This is supported by the fact that at higher ion fluxes the shape of the damage profiles deviate in a similar way from the calculated ones as for elevated temperatures (cp. Fig. 10 with corresponding figures in [25]). Is T_I too low for any defect mobility, no annealing will occur and, consequently, the ion flux does not influence the damage formation. Otherwise, at high enough temperatures mobile defects result in defect annealing, which is more effective at low ion fluxes. The consequence is that the damage concentration decreases with decreasing ion flux. This is demonstrated for GaAs in Fig. 4, which plots the damage concentration versus the ion fluence N_I for two different values of the ion flux j and two temperatures [26]. At $T_I = 100$ K no influence of j is observed, whereas at $T_I = 295$ K the damage concentration increases with rising j. This can be explained by the fact that a significant defect mobility in GaAs starts around 250 K only [27].

The given explanation of the effect of the ion flux on the damage formation is more intuitive and to some extent a simplification which holds well for moderate temperatures and reasonable fluxes used for common applications. Under extreme conditions as e.g. high temperatures *and* high ion fluxes or extremely high ion fluxes, the processes of damage formation become much more complicated, and pure ion-flux effects may also occur.

2.4. Ion energy

In Fig. 5 the number of displacements per ion and unit length, N^*_{displ}, is plotted versus the depth for Br ions implanted in GaAs with various energies. From the figure it is obvious that with

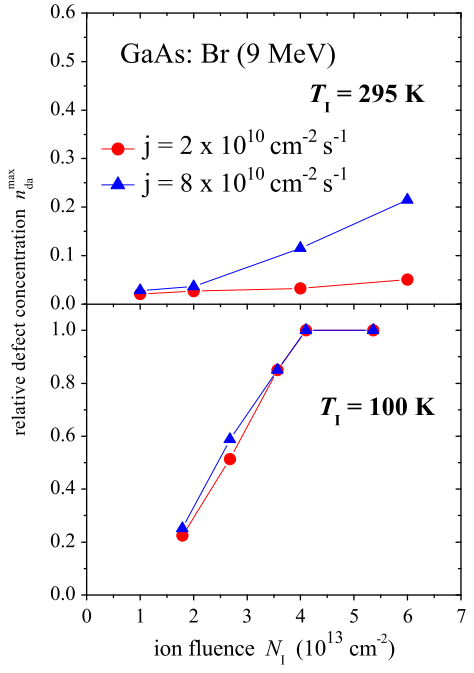

Fig. 4. Relative defect concentration in the maximum of the distribution, n_{da}^{max}, versus the ion fluence N_I for GaAs implanted with 9 MeV Br ions applying two different ion flux j at two different temperatures T_I.

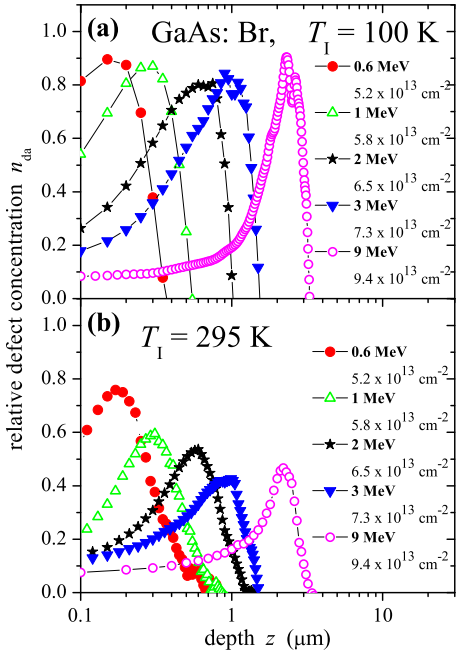

Fig. 6. Damage profiles $n_{da}(z)$ for GaAs implanted with Br ions of various energies at $T_I = 100$ K (a) and $T_I = 295$ K (b). For each temperature, the ion fluences were chosen to obtain the same number of displacements per lattice atom in the maximum of the distribution for all energies applied. Notice the logarithmic depth scale.

increasing ion energy the maximum of the distribution shifts into larger depths. This is because the nuclear energy loss occurs at the end of the range of the implanted ions, when their current energy undergoes a certain value. Before this, the electronic energy loss is the dominating process. Furthermore, the maximum value decreases due to the enhanced straggling of the high-energetic ions. One has to keep in mind that the distributions shown in Figs. 1 and 5 are mean values for one ion resulting from the calculation for very many ions. It is worth mentioning that the decrease of the maximum values of N^*_{displ}, which is visible in both Figs. 1 and 5, has a completely different physical origin. In Fig. 1 different ion species are regarded and the maximum value of N^*_{displ} is closely related to the density of the collision cascades of the individual ions. In Fig. 5 all calculations are performed for Br ions, i.e. the density of the collision cascades at the end of the range of the individual ions is always the same. And, as already mentioned, the straggling of the ions, which increases with rising energy, finally causes the reduction of the maximum of N^*_{displ}. To study the influence of the ion energy on the damage formation, Br ions were implanted into GaAs with various energies between 0.6 MeV and 9 MeV. For each energy the ion fluence was chosen to reach equal n_{dpa} values in the maximum of the distribution, i.e. an equal energy density deposited in nuclear processes. The results of these experiments are plotted in Fig. 6 which shows the damage profiles for implantation at (a) $T_{\mathrm{I}} = 100$ K and (b) $T_{\mathrm{I}} = 295$ K [26]. In the case of $T_I = 100$ K for all ion energies applied, almost the same maximum damage concentration is found. This means that no special effect of the energy is seen (see also [28]). In contrast, for implantation at room temperature the maximum damage concentration decreases with increasing ion energy, although the ion fluences were adjusted to obtain equal n_{dpa} values. To understand these findings one has to think about what the enhanced straggling at higher ion energies means, because this is the main effect of the ion energy. Let us consider a certain voxel within the sample close to the maximum of the distribution. For a low ion energy this voxel is much more often struck by ions than for a high ion energy due to the larger straggling in the latter case. In other words, the enhanced straggling of the ions over the depth results in a reduction of the local ion flux at a fixed depth. This so-called local ion flux decreases with increasing ion energy (providing an equal (real) ion flux for all energies). Then the results in Fig. 6 mean that at $T_{\mathrm{I}} = 100$ K the local ion flux is not important, whereas it is important at room temperature. This finding is in very good agreement with the results obtained when varying the (real) ion flux as shown in Fig. 4. Therefore, it can be concluded that the effect of the ion energy on the damage formation in GaAs can be explained by the local ion flux. Similar results are to be expected for other semiconductors too.

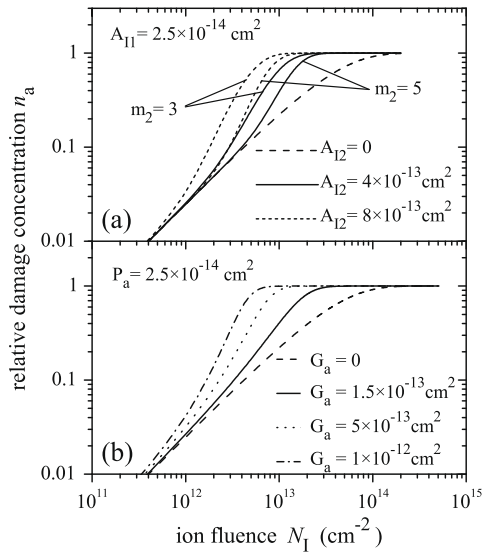

Fig. 7. Model curves of the relative amount of amorphous material, n_{a}, versus the ion fluence N_{I} calculated with Eq. (3) (upper part) and Eq. (4) (lower part). Both equations account for direct impact amorphization and stimulated growth of already existing amorphous regions.

2.5. Ion fluence

The ion fluence is the number of ions implanted per unit area in the material and is given by the product of the (usually constant) ion flux and time. Consequently, the damage concentration versus the ion fluence represents a time dependence and comprises information about the mechanisms of damage formation. Therefore, numerous models were developed to describe the fluence dependence of the damage concentration [29–35]. A more recent review is given in [36]. The fluence dependence is analysed at a fixed depth, usually in the maximum of the damage distribution. In this case the volume damaged by one ion can be approximated by a cylinder of low height like a slice cut out of the collision cascade at that particular depth parallel to the surface. If each ion produces an amorphous cylinder, the layer is completely amorphized when the whole area is struck by these cylinders. This can be represented by the rate equation

$$\frac{dn_{\mathrm{a}}}{dN_{\mathrm{I}}} = P_{\mathrm{a}}(1 - n_{\mathrm{a}}), \tag{1}$$

where n_{a} is the relative amount of damage (amorphous fraction), P_{a} is the cross section for the formation of amorphous material per ion and $(1 - n_{\mathrm{a}})$ is the probability to strike still undamaged material. For Eq. (1) the analytical solution is

$$n_{\mathrm{a}} = 1 - \mathrm{e}^{-P_{\mathrm{a}}N_{\mathrm{I}}}. \tag{2}$$

Taking into account an inner structure of the damaged cylinder consisting of an amorphous core with the area A_{I1} surrounded by a weakly damaged area A_{I2} which becomes amorphous only after being struck by $m_2 + 1$ ions, one obtains [32,37]

$$n_{\mathrm{a}} = 1 - \sum_{k=0}^{m_2} \frac{(A_{\mathrm{I2}}N_{\mathrm{I}})^k}{k!}\mathrm{e}^{-(A_{\mathrm{I1}}+A_{\mathrm{I2}})N_{\mathrm{I}}}. \tag{3}$$

Without an amorphous core, i.e. for $A_{\mathrm{I1}} = 0$, one obtains the classical overlap damage model [29]. The amorphization of the outer area A_{I2} after being struck by several ions can be also interpreted as a stimulated amorphization, i.e. a stimulated growth of already existing amorphous regions. This can be easily incorporated in Eq. (1) and one obtains

$$\frac{dn_{\mathrm{a}}}{dN_{\mathrm{I}}} = (P_{\mathrm{a}} + G_{\mathrm{a}}n_{\mathrm{a}})(1 - n_{\mathrm{a}}). \tag{4}$$

In the product $G_{\mathrm{a}}n_{\mathrm{a}}$, G_{a} is a measure for the strength of the stimulated growth, and n_{a} takes into account that growth can take place only if already amorphous regions exist. In Eq. (3) A_{I1} corresponds to P_{a} and the stimulated growth is controlled by A_{I2} and m_2. Fig. 7 depicts some model curves calculated with Eq. (3) (part a) and with Eq. (4) (part b). As discussed above, both equations follow from similar physical assumptions and this reflects in the calculated curves which exhibit a very similar structure. At very low ion fluences the damage concentration is governed by the parameter P_{a} only. This is the fluence range where almost each ions strikes still crystalline material and the collision cascades of individual ions do not overlap. Therefore, the quantity P_{a} yields the effect of a single ion impact in virgin material. Stimulated amorphization becomes prominent at higher ion fluences for which the collision cascades start to overlap. It is worth mentioning that a precise determination

of P_a requires experimental data for sufficiently low ion fluences. Further, from a successful fit with Eq. 4 it cannot be concluded that a single ion impact produces fully amorphized regions, but at least heavily damaged material. Examples for the use of Eq. (4) are given in Section 4. For $P_a \ll G_a$ the damage formation is dominated by the growth of amorphous material whereas the direct impact amorphization is negligible. In this case P_a can be regarded as a substitute for nucleation of amorphous seeds and amorphization of the layer is then achieved by the nucleation of amorphous seeds and their rapid growth during subsequent implantation. Such a model was suggested for Si in [35] and successfully applied also to SiC [38]. Amorphization by nucleation and growth is especially relevant to describe amorphization at elevated temperatures (see Section 6 and [34]) or in special materials (see Sections 7.1 and 7.2).

If only point defects are produced within a single ion impact, the overlap of the collision cascades may result in a recombination of defects, i.e. the annihilation of vacancies and interstitial atoms. The consequence is a saturation of the measured defect concentration at a rather low level due to the balance between defect production and defect recombination. This mechanism is taken into account by the first term of the following equation:

$$\frac{dn_{pd}}{dN_I} = (P_{pd} - R_{pd} n_{pd}) + C n_{pd}^{\alpha}\left(1 - \frac{n_{pd}}{n_{pd}^{*}}\right) = P_{pd} e^{-R_{pd} N_I} + C n_{pd}^{\alpha}\left(1 - \frac{n_{pd}}{n_{pd}^{*}}\right), \quad (5)$$

where n_{pd} is the relative concentration of point defects, P_{pd} is the cross section for point defect production and R_{pd} the parameter for defect recombination. In some cases the exponential function contains $(R_{pd}N_I)^2$ instead of $R_{pd}N_I$ to reach the equilibrium between defect production and recombination within a narrower range of ion fluences [34]. The second term in Eq. (5) characterizes the formation of non-recombinable clusters of point defects with the parameter C up to a saturation concentration of n_{pd}^{*}. The exponent α is usually 1 but it can be increased to achieve n_{pd}^{*} within a smaller fluence range. To show the influence of the parameters in Eq. (5), Fig. 8 depicts typical model curves with $\alpha = 1$. The solution of differential equations like Eqs. (4) or (5) can be easily obtained by numerical methods.

Provided the experimental technique is sensitive to both amorphous and heavily damaged areas and point defects, as it is the case for e.g. optical measurements and RBS, Eqs. (4) and (5) can be combined and one obtains [34]

$$\frac{dn_{pd}}{dN_I} = P_{pd} e^{-R_{pd} N_I}(1 - n_a) + C n_{pd}^{\alpha}\left[1 - \frac{n_{pd}}{n_{pd}^{c}(1 - n_a)}\right] - \frac{dn_a}{dN_I}\frac{n_{pd}}{1 - n_a}, \quad (6)$$

$$\frac{dn_a}{dN_I} = (P_a + G_a n_a)(1 - n_a).$$

These formulas describe a three-step amorphization (see model calculations in Fig. 9), which typically occurs in GaN (see [39] and Section 7.2). Eq. (6) is also successfully applied to Si (see [40] and references therein) and III–V compounds implanted at elevated temperatures (see Section 6), and to AlAs (see Section 7.1).

In principle, also other mechanisms can be transferred into differential equations (see e.g. [41]). However, one always has to keep in mind to which types of damage the method applied is sensitive and whether the data contain enough information (structure) to unambiguously determine the free parameters of the corresponding model.

Finally it should be mentioned that the effect of the other implantation parameters (especially of ion mass, ion flux and implantation temperature) are present in the model parameters.

3. Implantation temperature and concept of critical temperatures T_c

The explanation of the relevant parameters in Sections 2.2–2.4 demonstrated already that the target temperature during implantation, T_I, is a very crucial parameter for the damage formation. Therefore, a separate section is devoted to T_I, which is arranged in three parts: a first part about the modelling, a second part with experimental results, and a short conclusion.

3.1. Defect-out-diffusion model

As mentioned at the beginning of Section 2.5, the volume damaged by one ion at the depth of maximum damage can be approximated by a thin cylinder with the area $A_I = \pi R^2$ (R radius of the cylinder) parallel to the surface. If each ion produces an amorphous cylinder, the layer is completely amorphized when the whole area is struck by these cylinders. That means the critical ion fluence necessary for amorphization (referred to as amorphization fluence) N_I^{am} is proportional to $1/A_I$. An amorphization fluence for reference can be defined, which is measured at very low temperatures (in principle at $T_I = 0$ K), at which no defect annealing occurs, and is

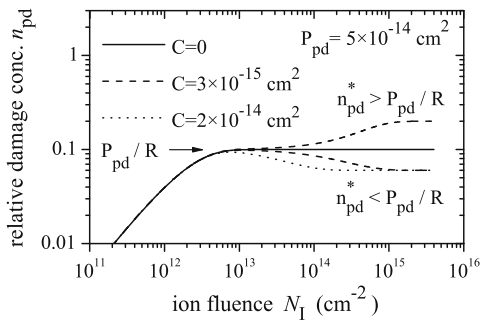

Fig. 8. Model curves of the relative amount of point defects, n_{pd}, versus the ion fluence N_I calculated with Eq. (5). The model takes into account the formation of point defects within the single ion impacts, the recombination of defects, occurring when the collision cascades of the individual ions start to overlap and, finally, the formation of non-recombinable clusters of point defects with a certain saturation concentration n_{pd}^{*}.

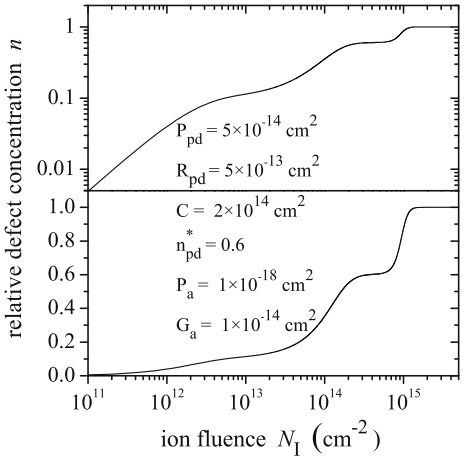

Fig. 9. Model curves of the relative defect concentration n versus the ion fluence N_I calculated with Eq. (6) and $n = n_a + n_{pd}$. For clarity the results are plotted in a double logarithmic scale (upper part) and a half-logarithmic scale (lower part).

given by $N_I^0 \propto R_0^{-2}$. For a given material N_I^0 only depends on the ion species, i.e. on N^*_{displ}, the number of displacements per ion and unit length. At higher temperatures T_I, defects can diffuse within the collision cascade and recombine at its outer regions, thus yielding a reduction of the radius of the damaged area to $(R_0 - \delta R)$. The ratio $N_I^{\mathrm{am}}(T_I)/N_I^0$ is then given by

$$\frac{N_I^{\mathrm{am}}(T_I)}{N_I^0} = \frac{R_0^2}{(R_0 - \delta R_0)^2} = \left(1 - \frac{\delta R_0}{R_0}\right)^{-2}. \tag{7}$$

Because thermally enhanced diffusion is assumed to have caused the shrinkage of the area damaged by one ion, the following ansatz for δR is made:

$$\delta R = L_0 \exp\left(-\frac{E_a}{2k_B T_I}\right), \tag{8}$$

where k_B is the Boltzmann constant. Using Eqs. (7) and (8) one obtains [30,31]

$$\frac{N_I^{\mathrm{am}}(T_I)}{N_I^0} = \left[1 - \frac{L_0}{R_0}\exp\left(-\frac{E_a}{2k_B T_I}\right)\right]^{-2} \tag{9}$$

with the free parameters E_a being the activation energy of the diffusion process, L_0 the diffusion length at $T_I \to \infty$ (representing the strength of annealing) and R_0 depending on the ion mass or N^*_{displ}, respectively. If one would assume the clusters to be spherical instead of cylindrical, the exponent -2 in Eq. (9) would change to -3. A similar result with

$$\frac{N_I^{\mathrm{am}}(T_I)}{N_I^0} = \left[1 - \frac{A_a}{jP_a^*}\exp\left(-\frac{E_a}{k_B T_I}\right)\right]^{-1} \tag{10}$$

is obtained when starting from a differential equation as in Eq. (1) and incorporating a temperature dependent defect annealing with the parameter A_a [42]

$$\frac{dn_a}{dN_I} = \left[jP_a^* - A_a \exp\left(-\frac{E_a}{k_B T_I}\right)\right](1 - n_a). \tag{11}$$

In contrast to Eq. (1), here the dependence on the ion flux is explicitly considered by $P_a = jP_a^*$ (note that P_a^* has another dimension than P_a). From Eqs. (9) and (10) a critical temperature T_c can be deduced for which the amorphization fluence reaches infinity, which is given by

$$T_c = \frac{E_a}{2k_B \ln\left(\frac{L_0}{R_0}\right)} \tag{12}$$

and

$$T_c = \frac{E_a}{k_B \ln\left(\frac{A_a}{jP_a^*}\right)}. \tag{13}$$

Within the defect-out-diffusion model, implantation at $T_I = T_c$ means that $\delta R = R_0$ is valid and thus no defects should remain.

3.2. Experimental results

It turns out that for a wide range of materials the amorphization fluence as a function of the implantation temperature is very well represented by Eqs. (9) or (10). In most cases the amorphization fluence is determined by TEM or from RBS measurements. Fig. 10 shows the damage profiles as determined from RBS measurements on InP implanted with Si ions at different temperatures. amorphization is reached for $n_{da} = 1$, here taken at the depth of maximum damage concentration. The resulting N_I^{am} values are plotted in Fig. 11 together with further data for InP [23]. The lines are fitted to the experimental data using Eq. (9) and, as can be seen from the figure, a good fit is obtained for all ion species applied. Similar

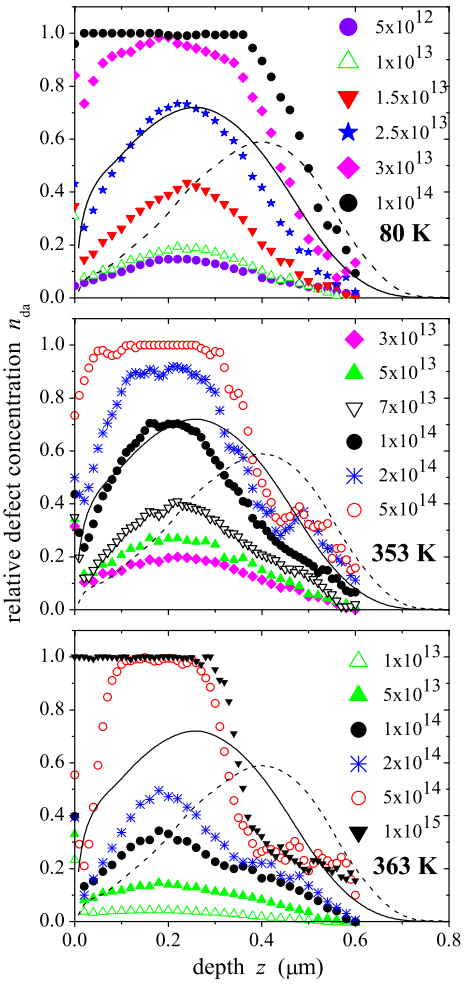

Fig. 10. Damage profiles $n_{da}(z)$ for InP implanted with 300 keV Si ions and various ion fluence N_I given in cm^{-2}. Implantation was performed at 80 K (upper part), 353 K (middle part) and 363 K (lower part). For comparison, the primary displacements (solid lines) and the ion distributions (dashed lines) are given in arbitrary units.

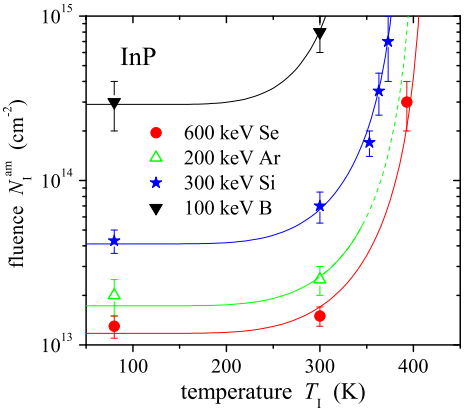

Fig. 11. Critical ion fluence necessary for amorphization in the maximum of the damage distribution, N_I^{am}, versus the implantation temperature T_I for InP implanted with various ion species. The symbols are the measured data and the lines are calculated with Eq. (9), which assumes the reduction of the defect clusters produced by one ion due to a thermally enhanced diffusion and annihilation of point defects.

results can be also found for other semiconductors like Ge [30,43], Si [30,31,40], SiC (see e.g. [44]), GaAs [43] and InAs [45]. In some

materials for which enough data are available, T_c follows the empirical formula:

$$T_c = \frac{A}{B - \ln\left[\left(N^*_{\mathrm{displ}}\right)^2 j\right]} = \frac{A}{\ln\left[\frac{e^B}{\left(N^*_{\mathrm{displ}}\right)^2 j}\right]} \quad (14)$$

with N^*_{displ} given in displacements per ion and Å and j in ions per cm^2 and s. Eq. (14) was originally suggested for the reversal temperature T_R separating between ion-beam induced epitaxial crystallisation and ion-beam induced interfacial amorphization of an amorphous/crystalline interface [46]. Eq. (14) has a similar structure as the formulas resulting from the modelling (Eqs. (12) and (13)). It is interesting to note that the dependence of the ion flux j matches the one of the model prediction in Eq. (13). A and B are free parameters. Available data for T_c, A and B for various III–V semiconductors are summarised in [47]. Remarkable is that the lower limit of T_c is successfully correlated with known annealing stages of intrinsic defects in the corresponding crystalline material [48], which – at least to some extent – supports the defect-out-diffusion model.

It should be mentioned that the activation energies following when fitting the amorphization fluence as a function of the implantation temperature with Eqs. (9) are all around 0.3 eV (InP: (0.33–0.35) eV [23]; GaAs: 0.29 eV and Ge: 0.26 eV [43]; SiC: 0.24 eV [49]; Si: (0.20–0.26) eV) [31]). However, when the correlation between the critical temperature T_c and $(N^*_{\mathrm{displ}})^2 j$ is analysed (see Eq. 14), activation energies E_a with $E_a = Ak_B$ of around 1 eV are obtained [45,47]. Despite the fact that these activation energies are difficult to interpret, since they describe the diffusion of intrinsic defects during the irradiation, the difference between the two differently obtained values is not yet understood.

3.3. Conclusion

One advantage of the concept of critical temperatures is that the formation of radiation damage in semiconductors can be systematized. It will be shown in Sections 4–6 that a similar behaviour for many semiconductors is found depending on whether the implantation temperature T_I is $T_I \ll T_c$, $T_I < T_c$ or $T_I \approx T_c$, although in reality there is no sudden but, rather continuous transition between the three regions. If the parameters A and B appearing in Eq. (14) are determined for a given material then the critical temperature can be calculated for each implantation condition. N^*_{displ} follows from the chosen ion mass and ion energy. Having the ion flux fixed according to the desired ion fluence, T_c can be calculated and with that the damage formation to be expected at a certain temperature can be estimated.

4. Damage formation at $T_I \ll T_c$

If the ion implantation is performed at very low temperatures, thermal effects can be widely excluded. At the Institut für Festkörperphysik in Jena an experimental setup is available which allows for conducting the irradiation and the subsequent RBS analysis at about 15 K without changing the target temperature or the environment of the sample [50]. In this case the condition before-mentioned is reasonably fulfilled and ion-beam induced effects can be easily studied.

At such low temperatures a good agreement of the shape of the depth distribution of damage is found between measurement and SRIM calculation. This can be seen in Fig. 2 for ion-implanted GaAs. A similarly good agreement was found for InP (see upper part of Fig. 10) and Ge [51]. Surprisingly the agreement seems to be slighter for Si [52], which was also seen at room temperature [53]. The reason for this is not yet clear and further studies are desirable.

Now the fluence dependence of the damage concentration at the depth of the maximum is investigated. The results for various ion species implanted in GaAs are given in Fig. 12 [54]. One can see that for all ion species the curves $n^{\max}_{da}(N_I)$ have the same structure. They can be modelled assuming a direct impact damaging with the cross section P_a and stimulated growth of damage which exists from previous ion-implantation, with the parameter G_a (see Eq. (4)). As to be expected the parameters P_a and G_a increase with rising ion mass. Additionally, P_a increases more strongly with ion mass than G_a. Fig. 13 plots the same results as in Fig. 12 but versus n_{dpa}, the number of displacements per lattice atom, i.e. versus a normalised ion fluence (see Section 2.5). Only for ions heavier than Ar a uniform dependence for the various ion species is found. In these cases the amount of damage is solely determined by the energy density deposited into collision processes. For lighter ions a significantly higher energy density has to be deposited to obtain the given amount of damage. This is also observed in InP and GaP [47]. And the comparison of damage produced by He and Ar ions in Si or Ge yields the same behaviour [52]. The reason for this is not yet fully understood. It suggests that non-linear processes occur within the lifetime of the collision cascade. Another point to be mentioned is the electronic energy loss of the implanted ions, which may change the charge state of defects and thus their mobility, which could promote some in-cascade annealing. In the case of the light elements the ratio between electronic and nuclear energy loss is higher than for heavier ions, thus the annealing may be more efficient in this case.

The results for $T_I \ll T_c$ can be summarised as follows: (i) There is a reasonable agreement between measured and calculated depth distributions of damage with respect to the shape of the profiles and the position of the maximum. (ii) Above a certain ion mass (or value of N^*_{displ}) a constant energy deposition in nuclear processes per volume renders the materials amorphous whereas below, the necessary energy density increases with decreasing ion mass. (iii) No influence of the ion flux j is observed in that temperature range.

5. Damage formation at $T_I < T_c$

The closer the implantation temperature comes to T_c, the more the damage formation is influenced by annealing effects occurring within the lifetime of the collision cascades. This is clearly visible from the damage profiles plotted in Fig. 10 for ion-implanted InP. With rising implantation temperature two effects occur: (i) for a given ion fluence the maximum damage concentration decreases and (ii) the shape of the measured profiles deviates more and more from that of the calculated ones. The depth position of the

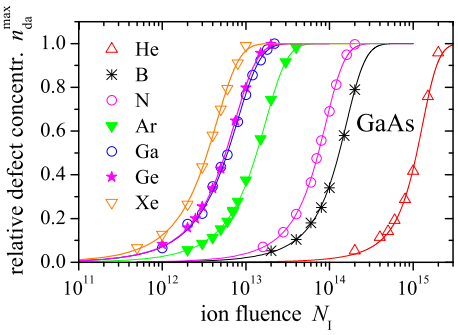

Fig. 12. Relative defect concentration in the maximum of the distribution, $n^{\max}_{da}$, versus the ion fluence N_I for GaAs implanted with various ion species. Implantation and subsequent RBS analysis were performed at 15–20 K. The lines are fitted to the experimental data using Eq. (4) which accounts for direct impact amorphization and stimulated growth of already existing amorphous regions.

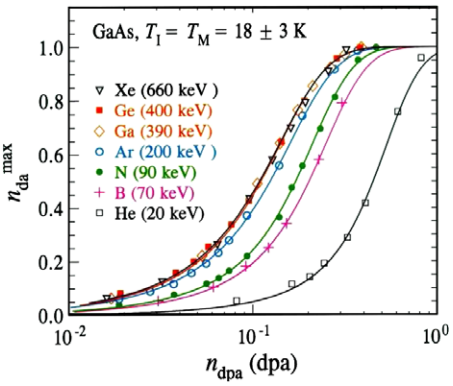

Fig. 13. Relative defect concentration in the maximum of the distribution, n_{da}^{max}, versus the number of displacements per lattice atom, n_{dpa}, for GaAs implanted with various ion species (see also Fig. 12).

maximum seems to shift to a lower depth, or the rearward part of the damage profile is missing. These findings suggest that the defect annealing during the implantation varies with depth and is most pronounced at the interface to the underlying crystalline substrate, either due to a recrystallisation process or the out-diffusion of defects into the substrate.

A similar deviation of the defect profiles from the calculated distributions, as discussed above, is found when the implantation is performed with a higher ion flux [25]. In many studies of the damage formation as a function of the ion flux, the integral damage (integral of the damage profiles over the depth) is analysed. It is found that for a given ion fluence the integral damage increases proportionally to j^n with $n \approx 0.15$–0.4 increasing with rising T_I [55,56], which means a reduced influence of j at lower temperatures. The increase of damage formation with increasing ion flux can be explained within the concept of critical temperatures. An increase of the ion flux results in a higher T_c. For a given temperature T_I this corresponds to a relative decrease of T_I in relation to T_c and this means more damage.

The complicated interplay of implantation temperature, ion flux and ion fluence is the material feature occurring in the temperature range $T_I < T_c$.

6. Damage formation at $T_I \approx T_c$

In the framework of the out-diffusion model (see Section 3.1), implantation at $T_I \approx T_c$ means that the reduction of the radius of the primary damage cylinder is in the order of the radius itself and, consequently, at least no heavily damaged or amorphous material should remain. And indeed, this behaviour is experimentally proved. Fig. 14 depicts the damage concentration versus the ion fluence N_I for three examples for which $T_I \approx T_c$ is fulfilled [47]. Similar curves are also measured for silicon ion implanted at the corresponding temperatures (see [40] and references therein). Fig. 14 shows that over a wide range of N_I the relative concentration is of the order of 0.1—0.15. This means, the predicted defect recombination occurs, but it is not perfect, leaving behind point defects or point defect complexes, which is also proven by TEM and optical measurements [57]. Amorphization is obtained for very large ion fluences $N_I > 10^{16}$ cm^{-2}. Before amorphization a defect band at the depth of maximum ion concentration is detected by TEM [23]. We believe that this defect band suppresses the diffusion of defects into the substrate, which results in a defect accumulation in depths of maximum nuclear energy deposition. Then amorphous seeds nucleate and grow rapidly during further implantation to form a closed amorphous layer in the depth of maximum nuclear energy deposition.

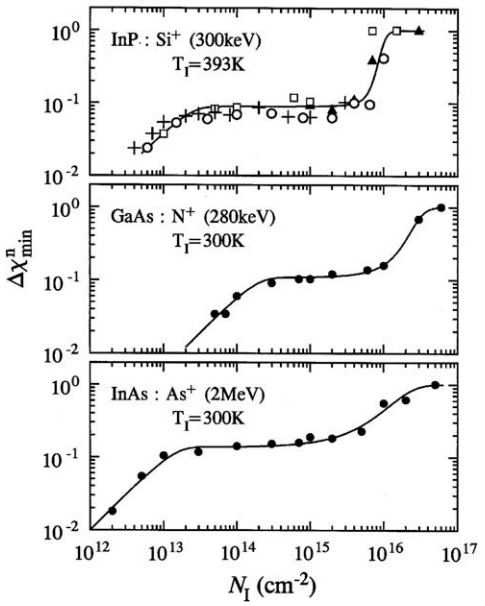

Fig. 14. Normalised difference in minimum yield $\Delta\chi^n_{min}$ in the maximum of the distribution (corresponding to the relative defect concentration n_{da}^{max}) versus the ion fluence N_I for implantation in InP (upper part), GaAs (middle part) and InAs (lower part) with conditions for which $T_I \approx T_c$ is fulfilled. The symbols are the experimental data and the lines are calculated assuming formation and recombination of point defects and nucleation and growth of amorphous zones (for details see Section 2.5).

7. Misfits

There are some materials whose behaviour does not fit into the concept of critical temperatures. Besides the semiconductors AlAs [58], GaN [6] and AlN [59] also the insulators MgO [60,61] and ZnO [22,62] (and probably many other insulators) belong to that group. Even at very low temperatures only point defects or point defect complexes are produced by a single ion impact in the corresponding crystalline materials, which recombine when the collision cascades start to overlap, thus resulting in a saturation of the defect concentration at rather low values of 0.02–0.15 depending on the material. However, this is the only joint feature because at high ion fluences, i.e. when the local ion concentration exceeds some critical value, each material shows a specific behaviour. As examples, results for AlAs and GaN are shown.

7.1. AlAs

Fig. 15 shows the defect concentration in the maximum of the measured distribution versus the ion fluence for Ar implanted AlAs [48]. Even for implantation at $T_I \approx 20$ K and immediate RBS measurement without temperature change of the sample, the defect concentration saturates at only $n_{da}^{max} \approx 0.15$ and remains constant over a wide range of ion fluences. Only at large fluences the amorphization of AlAs occurs, but within a narrow fluence range.

Although the curve $n_{da}^{max}(N_I)$ for AlAs looks very simi-lar to those in Fig. 14, the physics behind it is different. The results in Fig. 14 were obtained for implantation at $T_I \approx T_c$ and can be explained by a thermally enhanced defect diffusion. In the case of AlAs at $T_I \approx 20$ K no defects were found to be mobile [63]. Therefore, the resistance against ion-beam induced damage formation is an inherent property of AlAs and not caused by any thermal effects. In [64] it was shown that the AlAs did not amorphize because the strain did not reach the critical value for amorphization. In

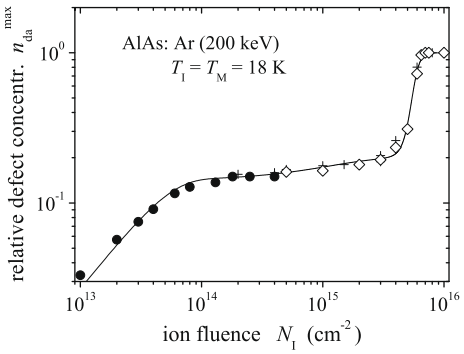

Fig. 15. Relative defect concentration in the maximum of the distribution, n_{da}^{max}, versus the ion fluence N_I for Ar ion-implanted AlAs with implantation and RBS analysis being performed at 18 K. The symbols are the experimental data and the line is calculated assuming formation and recombination of point defects and nucleation and growth of amorphous zones (for details see Section 2.5).

these studies the layer thickness was well below the projected range of the implanted ions. In our investigations amorphization of AlAs ($T_I \approx 20$ K) occurs, but in the depth of maximum ion concentration and not in that of maximum energy deposition into nuclear processes [58]. This is demonstrated in Fig. 16 for Na ion-implanted AlAs. The values of N_I^{am} obtained for different ion species reveal also no correlation with the nuclear energy density. On the contrary, a correlation with the atomic volume of the implanted ions was found. Our results suggest that amorphous seeds nucleate when the total volume introduced by the ions exceeds a critical value [48,65]. Possibly this causes a critical value of the strain necessary to nucleate amorphous seeds. These amorphous nuclei grow rapidly during further implantation due to ion-beam induced interfacial amorphization, thus causing the steep increase of n_{da}^{max} to $n_{da}^{max} = 1$ (see Fig. 15) and a rapid broadening of the amorphous layer (see Fig. 16).

7.2. GaN

In GaN, amorphization at $T_I = 15$ K proceeds in three steps. This can be seen in Fig. 17 which plots the damage concentration in the maximum of the measured distributions for a broad selection of ion species. At very low ion fluence independent of the ion species only point defects and point defect complexes are produced, the concentration of which depends on the energy density deposited in nuclear processes only (see Fig. 2(a)). When the collision cascades start to overlap, the balance between production and recombination limits the remaining defect concentration to a relatively low value of $n_{da}^{max} \leqslant 0.05$ over a wide range of ion fluences. With rising ion fluences a slight increase of n_{da}^{max} is observed suggesting that the defect recombination becomes less efficient. Furthermore, the defects extend more into the depth (not shown). A possible explanation of the observed behaviour is that the implanted ions attract and stabilise point defects and more complicated point defect complexes are formed. At a certain stage of this process (probably when the recombination efficiency reduces because of the imperfect structure of the surrounding lattice) the defect concentration increases up to a second intermediate plateau at $n_{da}^{max} \approx 0.7$, suggesting the transformation of defects into another type. This is expected to be a mixture of defect clusters and extended defects (most probably dislocation loops, see also [62]). Finally, amorphization is achieved by the nucleation and growth of amorphous material. This is illustrated in Fig. 18 showing the damage profiles for Ar ion fluences for which the transition to amorphousness is observed. The nucleation occurs neither at the depth of maximum nuclear energy deposition, nor at the depth of maximum ion concentration. The mechanism is not yet understood and seems to require a high concentration of both primary displacements and implanted ions.

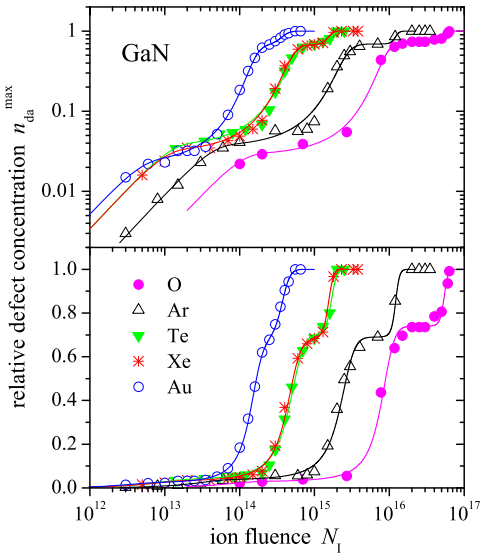

Fig. 17. Relative defect concentration in the maximum of the distribution, n_{da}^{max}, versus the ion fluence N_I for GaN implanted with various ion species. Implantation and subsequent RBS analysis were performed at 15 K. The lines are fitted to the experimental data taking into account formation and recombination of point defects, the formation of non-recombinable defect clusters and nucleation and growth of amorphous zones (for details see Section 2.5).

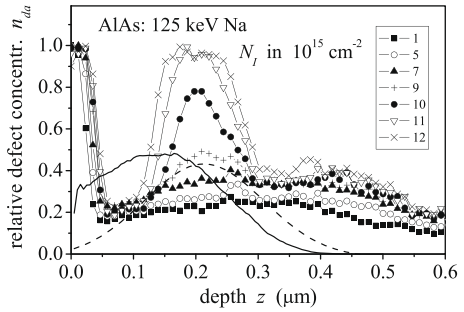

Fig. 16. Damage profiles $n_{da}(z)$ for Na ion-implanted AlAs with implantation and RBS analysis being performed at 18 K. The primary displacements (solid line) and the ion distribution (dashed line) are given for comparison in arbitrary units.

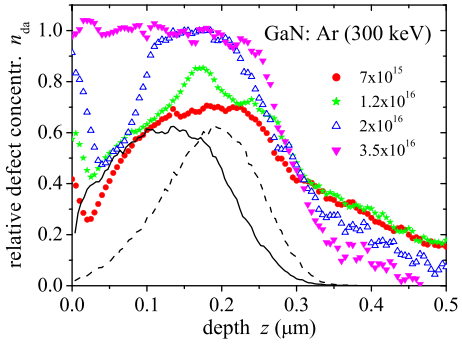

Fig. 18. Damage profiles $n_{da}(z)$ for Ar ion-implanted GaN with implantation and RBS analysis being performed at 15 K. The ion fluences are given in cm^{-2}. The primary displacements (solid line) and the ion distribution (dashed line) are given for comparison in arbitrary units.

8. Conclusion

There is still ongoing research to understand why the various materials, especially semiconductors, reveal variations in susceptibility to radiation damage produced by ion implantation. Experiments performed at 15 K without changing target temperature or environment provide a useful basis for this phenomenon. A closer look at III–V compounds shows that the cross section of damage production per ion P (see Eqs. (4) and (5)) is correlated neither to the ionicity, nor to elastic constants of the materials [66]. A good correlation is seen with a force constant derived from the optical lattice vibrations [54]. There are still many open questions and the study of ion-beam induced radiation damage in semiconductors and other materials remains a lively field of research.

References

[1] G. Götz, K. Gärtner (Eds.), High Energy Ion Beam Analysis of Solids, Akademie-Verlag, Berlin, 1988.
[2] J.R. Tesmer, M. Nastasi (Eds.), Hand Book of Modern Ion Beam Analysis, Materials Research Society, Pittsburgh, Pennsylvania, 1995.
[3] K. Gärtner, Nucl. Instr. and Meth. B 227 (2005) 522.
[4] J.F. Ziegler, J.P. Biersack, U. Littmark, The Stopping and Ranges of Ions in Solids, Pergamon, New York, 2003. <http://www.srim.org>.
[5] W. Wesch, A. Kamarou, E. Wendler, Nucl. Instr. and Meth. B 225 (2004) 111.
[6] E. Wendler, A. Kamarou, E. Alves, K. Gärtner, W. Wesch, Nucl. Instr. and Meth. B 206 (2003) 1028.
[7] B. Breeger, E. Wendler, Ch. Schubert, W. Wesch, Nucl. Instr. and Meth. B 148 (1999) 468.
[8] J. Nord, K. Nordlund, J. Keionen, K. Albe, Nucl. Instr. and Meth. B 202 (2003) 93.
[9] E. Wendler, W. Wesch, E. Alves, A. Kamarou, Nucl. Instr. and Meth. B 218 (2004) 36.
[10] K. Gärtner, Nucl. Instr. and Meth. B 252 (2006) 190.
[11] J.A. van Vechten, in: S.P. Keller (Ed.), Handbook of Semiconductors, Vol. 3, North Holland, 1980 (Chapter 1).
[12] R. Bäuerlein, Z. Phys. 176 (1963) 498.
[13] K. Thommen, Phys. Rev. 174 (1968) 938.
[14] R. Devanathan, W.J. Weber, J. Nucl. Mater. 278 (2000) 258.
[15] X. Kerbiriou, M.-F. Barthe, S. Esnouf, P. Desgardin, G. Blondiaux, G. Petite, J. Nucl. Mater. 362 (2007) 202.
[16] W. Jiang, W.J. Weber, S. Thevuthasan, D.E. McCready, Nucl. Instr. and Meth. B 148 (1999) 557.
[17] M.J. Caturla, T. Diaz de la Rubia, G.H. Gilmer, Mater. Res. Soc. Symp. Proc. 316 (1994) 111.
[18] J.J. Loferski, P. Rappaport, Phys. Rev. 111 (1958) 432.
[19] H. Flicker, J.J. Loferski, J. Scott-Monck, Phys. Rev. 128 (1962) 2557.
[20] W.L. Brown, W.M. Augustyniak, J. Appl. Phys. 30 (1959) 1300.
[21] S.J. Zinkle, C. Kinoshita, J. Nucl. Mater 251 (1997) 200.
[22] K. Lorenz, E. Alves, E. Wendler, O. Bilani, W. Wesch, M. Hayes, Appl. Phys. Lett. 87 (2005) 191904.
[23] E. Wendler, Th. Opfermann, P.I. Gaiduk, J. Appl. Phys. 82 (1997) 5965.
[24] For each material elevated means a different range of temperatures (see Section 3).
[25] E. Wendler, W. Wesch, G. Götz, Nucl. Instr. and Meth. B 52 (1990) 57.
[26] W. Wesch, E. Wendler, N. Dharmarasu, Nucl. Instr. and Meth. B 175–177 (2001) 257.
[27] A. Pillukat, K. Karsten, P. Ehrhart, Phys. Rev. B 53 (1996) 7835.
[28] R. Lauck, E. Wendler, W. Wesch, Nucl. Instr. and Meth. B 242 (2006) 484.
[29] J.F. Gibbons, Proc. IEEE 60 (1970) 1062.
[30] F.F. Morehead, B.L. Crowder, Radiat. Eff. 6 (1970) 27.
[31] J.R. Dennis, E.B. Hale, J. Appl. Phys. 49 (1978) 1119.
[32] G. Carter, R.P. Webb, Radiat. Eff. 43 (1979) 19.
[33] R.P. Webb, G. Carter, Radiat. Eff. 59 (1981) 69.
[34] N. Hecking, K.F. Heidemann, E. te Kaat, Nucl. Instr. and Meth. B 15 (1986) 760.
[35] S.U. Campisano, S. Coffa, V. Rainieri, F. Priolo, E. Rimini, Nucl. Instr. and Meth. B 80–81 (1993) 514.
[36] W.J. Weber, Nucl. Instr. and Meth. B 166–167 (2000) 98.
[37] N.A. Sobolev, Ph.D. Thesis, University of Jena, 1978.
[38] W. Bolse, Nucl. Instr. and Meth. B 148 (1999) 83.
[39] E. Wendler, A. Kamarou, E. Alves, K. Gärtner, W. Wesch, Nucl. Instr. and Meth. B 206 (2003) 1028.
[40] B. Pfeifer, J.K.N. Lindner, B. Rauschenbach, B. Stritzker, Nucl. Instr. and Meth. B 96 (1995) 150.
[41] C.S. Schnohr, E. Wendler, K. Gärtner, K. Ellmer, W. Wesch, J. Appl. Phys. 99 (2006) 123511.
[42] W.J. Weber, L.M. Wang, Nucl. Instr. and Meth. B 91 (1994) 63.
[43] T.E. Haynes, O.W. Holland, Appl. Phys. Lett. (1991) 452.
[44] E. Wendler, A. Heft, W. Wesch, Nucl. Instr. and Meth. B 141 (1998) 105.
[45] E. Wendler, N. Dharmarasu, E. Glaser, Nucl. Instr. and Meth. B 160 (2000) 257.
[46] V. Heera, T. Henkel, R. Kögler, W. Skorupa, Phys. Rev. B 52 (1995) 15776.
[47] E. Wendler, B. Breeger, Ch. Schubert, W. Wesch, Nucl. Instr. and Meth. B 147 (1999) 155.
[48] E. Wendler, in: J.L. Duggan, I.L. Morgan (Eds.), Proc. of the 17th International Conference on the Application of Accelerators in Research and Industry, AIP Conference Proceedings, Vol. 680, Melville, New York, 2003, p. 670.
[49] A. Heft, E. Wendler, T. Bachmann, E. Glaser, W. Wesch, Mater. Sci. Eng. B 29 (1995) 142;
A. Heft, Ph.D. Thesis, Friedrich-Schiller-Universität Jena, 1996.
[50] B. Breeger, E. Wendler, W. Trippensee, Ch. Schubert, W. Wesch, Nucl. Instr. and Meth. B 174 (2001) 661.
[51] M. Hayes, A. Schroeter, E. Wendler, W. Wesch, F.D. Auret, J.M. Nel, Phys. Status Solidi (b) 244 (2007) 1544.
[52] A. Schroeter, Diploma Thesis, University of Jena, 2007.
[53] E. Friedland, Nucl. Instr. and Meth. B 256 (2007) 193.
[54] E. Wendler, W. Wesch, in: B. Kramer (Ed.), Advances in Solid State Physics, Vol. 44, Springer-Verlag, Heidelberg, 2004, pp. 363–374.
[55] U.G. Akano, I.V. Mitchell, F.R. Shepherd, C.J. Miner, R. Rousina, Can. J. Phys. 70 (1992) 789.
[56] T.E. Haynes, O.W. Holland, Appl. Phys. Lett. 58 (1984) 62.
[57] E. Wendler, W. Wesch, G. Götz, Nucl. Instr. and Meth. B 52 (1990) 57.
[58] E. Wendler, B. Breeger, W. Wesch, Nucl. Instr. and Meth. B 175–177 (2001) 78.
[59] E. Wendler, W. Wesch, Nucl. Instr. and Meth. B 242 (2006) 562.
[60] E. Wendler, K. Gärtner, W. Wesch, Nucl. Instr. and Meth. B 257 (2007) 488.
[61] E. Wendler, K. Gärtner, W. Wesch, Nucl. Instr. and Meth. B 266 (2008) 2872.
[62] E. Wendler, O. Bilani, K. Gärtner, W. Wesch, M. Hayes, F.D. Auret, K. Lorenz, E. Alves, Nucl. Instr. and Meth. B 267 (2009) 2708.
[63] A. Gaber, H. Zillgen, P. Ehrhart, P. Partyka, J. Appl. Phys. 82 (1997) 5348.
[64] P. Partyka, R.S. Averback, D.V. Forbes, J.J. Coleman, P. Ehrhart, W. Jäger, Appl. Phys. Lett. 65 (1994) 421.
[65] B. Breeger, Ph.D. Thesis, University of Jena, 2000.
[66] E. Wendler, L. Wendler, in preparation.